Hindawi
Mathematical Problems in Engineering
Volume 2018, Article ID 7482753, 10 pages
https://doi.org/10.1155/2018/7482753

Research Article

Cosine Matching Imaging Method for Rotating Scanning Synthesis Aperture Imaging Radiometer

Jianfei Chen,[1,2] **Xiaowei Zhu**,[1] **Sheng Zhang**,[2] **and Yuanjiang Li**[3]

[1] *School of Information Science and Engineering, Southeast University, Nanjing 210096, China*
[2] *School of Electronic and Optical Engineering, Nanjing University of Posts and Telecommunications, Nanjing 210046, China*
[3] *Institute of Electronic and Information, Jiangsu University of Science and Technology, Zhenjiang 212000, China*

Correspondence should be addressed to Jianfei Chen; chenjf@njupt.edu.cn

Received 23 May 2018; Accepted 9 September 2018; Published 26 September 2018

Academic Editor: Petr Páta

Millimeter-wave synthesis aperture imaging radiometer (SAIR) can realize high-resolution observations without requiring the real large aperture antenna. Among the SAIRs, the Rotating Scanning SAIR (RS-SAIR) with linear sparse array is a popular system with low redundancy and high reliability. However, due to the lack of matched imaging methods, its imaging precision is usually low. For improving its imaging precision, a novel Cosine Matching Imaging (CMI) method is proposed in this paper. In CMI method, according to the characteristic of rotating projection imaging, the angle-orientation image is constituted by the 1D projection images measured by RS-SAIR in a series of angles firstly. Then, according to the trajectory of the target in angle-orientation image, the pixel values of the brightness temperature image are extracted by cosine matching method from the angle-orientation image one by one. The simulation results demonstrate that the proposed CMI imaging method has higher reconstruction accuracy for the RS-SAIR.

1. Introduction

Millimeter-wave synthesis aperture imaging radiometers (SAIR) are powerful sensors for high-resolution observations in various fields [1–3]. By the aperture synthesis technique, SAIR can utilize some small antennas to constitute a large aperture antenna and realize high-resolution imaging observation. Each complex correlation of pairwise antennas is a sample of visibility function, which can be utilized to reconstruct the brightness temperature image of the target scene. Thus, the antenna array configuration is an extremely important component for the SAIR. It directly defines the distribution of the visibility samples and further affects the imaging performance of SAIR system. In fact, how to utilize fewer antennas to achieve the better imaging performance (i.e., array optimization) is always a difficult problem for the SAIR design. Since the first SAIR (ESTAR) developed in 1980s [4, 5], various array configurations have been proposed. Such as 2D rectangular array, sparse "Y" array, "U" array, circular array, and other arrays [6–15]. All of these arrays are looking for achieving the optimal array with low redundancy and larger synthesis aperture constituted by fewer antennas. Unfortunately, there is no effective optimization array which was proposed for 2D SAIR at present. Many antennas are needed for those 2D arrays, which result in high redundancy and system costs.

For utilizing antennas effectively and reducing systematic complexity, the scanning SAIRs with sparse array are proposed and applied in some SAIRs [13–17]. Among these SAIRs, the Rotating Scanning SAIR (RS-SAIR) with linear sparse array is the most popular system with low redundancy and high reliability. However, the existing imaging methods may not be accurate enough for some special applications. The sampling points of RS-SAIR is circularly distributed, which is unsuitable for traditional FFT-based methods. In order to deal with these visibility functions with irregular distribution, the Gridding and Nonuniform FFT (NUFFT) methods are proposed for the irregular SAIRs [18–21]. But due to the problem of insertion and resampling, some unnecessary errors will be introduced to the reconstructed images

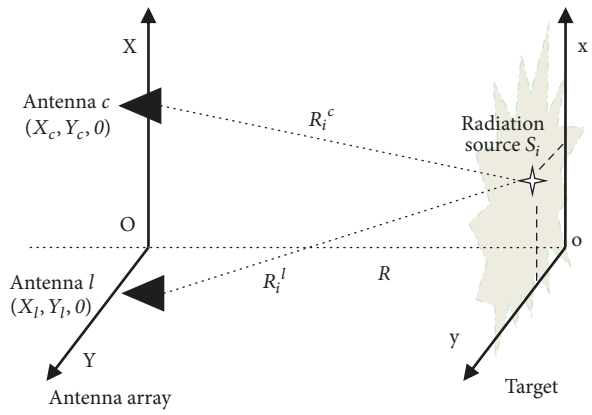

Figure 1: Geometry diagram of 2D synthetic aperture imaging.

inevitably. Therefore, the effective high-precision imaging method is to find the appropriate inverse method to reconstruct the target images from the irregular visibility function directly. Fortunately, the sampling points of RS-SAIR in radial direction are equispaced and suitable for applying FFT. The 1D radial projection images can be reconstructed by FFT-methods firstly, for example, the back projection (BP) method first to reconstruct the 1D projection images by FFT-methods and then compound the 2D scene images by the back projection operation according to the measuring angle of 1D images [22–24]. But due to the limitations of back projection, BP method cannot effectively deal with the aliasing problem between targets, especially for near-field with wider point spread function (PSF) and serious interference between targets [24–26]. For improving the imaging precision of RS-SAIR further, we study the synthesis aperture projection imaging principle deeply and find that the trajectory of targets in angle-orientation image meets cosine distribution. Based on this fact, a novel Cosine Matching Imaging (CMI) algorithm based on the CLEAN idea is proposed in this paper. In CMI method, the 1D projection images of 2D target scene are measured by the RS-SAIR with linear sparse array in a series of angles firstly. Then, the 1D projection images are arranged to constitute an angle-orientation image according the corresponding array angle. Finally, the pixel values of the brightness temperature image are extracted by the cosine matching method one by one from the angle-orientation image. The numerical simulation results demonstrate that the proposed CMI method can well reconstruct the millimeter images from RS-SAIR with fewer antennas. Its imaging accuracies is better than the BP method under the same conditions.

2. The Basic Synthesis Aperture Imaging Theory

Before the description of CMI method for RS-SAIR, the basic synthesis aperture imaging theory is demonstrated here. As Figure 1 shows, the antennas are located on *OXY*, the extend radiation source S is located on *oxy*, and its brightness temperature image is *T(x,y)*. The radiation source S is dispersed into N small parts. The distances between the i-th radiation source S_i and antennas c and l are R_i^c and R_i^l, respectively.

The correlation between the received signals E_c and E_l of pairwise antennas *(c, l)* is a sample of the so-called visibility function. According to [27], the visibility samples measured by pairwise antennas *(c, l)* can be expressed as

$$\begin{aligned} V_{c,l} &= \left\langle E_c\left(R_i^c, t\right) \bullet E_l^*\left(R_i^l, t\right)\right\rangle \\ &= \sum_{i=1}^{N} T\left(x_i, y_i\right) F_c\left(x_i, y_i\right) F_l^*\left(x_i, y_i\right) r_{c,l} e^{-jk\left(R_i^c - R_i^l\right)} \end{aligned} \tag{1}$$

where $< \bullet >$ denotes time integration operation, (x_i, y_i) is the coordinate of the point target S_i, T is the modified brightness temperature, $F(\bullet)$ is the normalized antenna pattern, $k = 2\pi/\lambda$ is angular wavenumber, and $r_{c,l}$ is the so-called fringe-wash function [28].

The $\exp[-jk(R_i^c - R_i^l)]$ denotes the phase difference of two antennas, which is the key factor for the synthetic aperture imaging. According to Figure 1, the distance R_i^c and R_i^l through Taylor expansion can be expressed as

$$\begin{aligned} R_i^c &= \sqrt{\left(x_i - X_c\right)^2 + \left(y_i - Y_c\right)^2 + R^2} \\ &\approx R + \frac{\left[\left(x_i - X_c\right)^2 + \left(y_i - Y_c\right)^2\right]}{2R} \end{aligned} \tag{2}$$

$$R_i^l \approx R + \frac{\left[\left(x_i - X_l\right)^2 + \left(y_i - Y_l\right)^2\right]}{2R} \tag{3}$$

Substitute (2) and (3) into (1), and define the spatial coordinates $u=k(X_l-X_c)/R$, $v=k(Y_l-Y_c)/R$. We can get the relation between visibility function and the brightness temperature image as

$$V(u, v) = e^{-j\varphi(u,v)} \iint T(x, y) F_c F_l^* r_{c,l} e^{-j(xu+yv)} dxdy \tag{4}$$

where $\varphi(u, v)=k(X_c^2+Y_c^2-X_l^2-Y_l^2)/2R$ is the phase-modified item, which can improve the imaging accuracy for the near-field SAIR effectively. For the ideal SAIR with identical receivers and antennas, the decorrelation effects $r_{c,l}\approx 1$ and antenna pattern $F(\bullet)$ can be ignored simply. Then (4) can be rewritten as follows:

$$V(u, v) = e^{-j\varphi(u,v)} \iint T^O(x, y) e^{-j(xu+yv)} dxdy \tag{5}$$

$$T^O(x, y) = \iint \left[V(u, v) e^{j\varphi(u,v)}\right] e^{j(xu+yv)} dudv \tag{6}$$

where $T^O(x, y)$ is the approximate brightness temperature image. For the complete visibility function $V(u, v)$ measured by the SAIR with "T" array, the brightness temperature image $T^O(x,y)$ can be reconstructed by the FFT-based methods as an approximate solution of $T(x,y)$. Such as the Modified-FFT (MFFT) imaging method, the brightness temperature images T^{MF} are reconstructed by Fourier transform from the visibility function with phase-modified item directly [26].

$$T^{MF} = FT\left[V(u, v) e^{j\varphi(u,v)}\right] \tag{7}$$

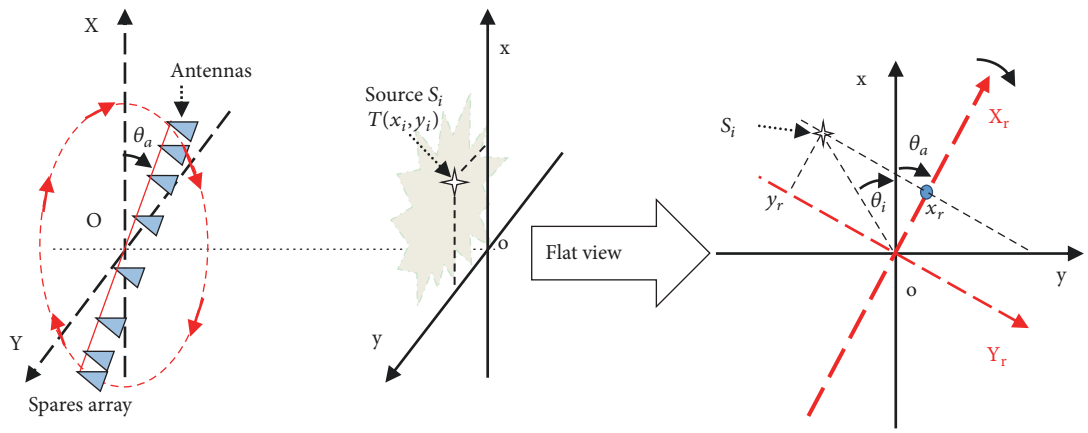

FIGURE 2: Geometry diagram of synthetic aperture projection imaging.

3. Description of CMI Method for RS-SAIR

For utilizing the antennas more effectively, RS-SAIR only uses a sparse linear array with fewer antennas to detect the 2D target scene. Its basic imaging theory is the aperture synthesis technology also, but the signal processing and imaging steps are different to other SAIRs. Its measuring principle is illustrated in Figure 2. The spares array is placed in the XOY plane and rotated around the center point O. θ_a is the array rotation angle.

For the sparse array with given θ_a, its spatial coordinates $u=k(X_l-X_c)/R$, $v=k(Y_l-Y_c)/R=0$ under X_rOY_r coordinates, and the coordinates of targets should be transformed to the projection coordinates (x_r, y_r), which are the change of rotation angle θ_a. Then the visibility function $V_{\theta a}(u, v)$ measured by the linear array with given θ_a can be rewritten as

$$\begin{aligned} V_{\theta a}(u,0) &= e^{-j\varphi(u,0)} \iint T(x_r, y_r)\, e^{j(x_r u + y_r 0)} dx_r dy_r \\ V_{\theta a}(u)\, e^{j\varphi(u)} &= \int \left[\int T(x_r, y_r)\, dy_r \right] e^{-j(x_r u)} dx_r \\ &= \int T^P_{\theta a}(x_r)\, e^{-j(x_r u)} dx_r \end{aligned} \tag{8}$$

where x_r is the projection coordinate on the X_r axis (paralleling to the sparse array at angle θ_a); y_r is the projection coordinate on the Y_r axis. $T^P_{\theta a}(x_r) = \int T(x_r, y_r) dy_r$ is the 1D projection image, which can be reconstructed by the 1D MFFT method as the following formula:

$$T^P_{\theta a}(x_r) = FT_1 \left[V_{\theta a}(u)\, e^{j\varphi(u)} \right] \tag{9}$$

However, the value of 1D projection image T_P is a synthetic value containing all the pixels with the same y_r coordinate under angle θ_a. The targets distributed along the Y_r axis will be concealed for each other and hardly to be distinguished. Thus, the large reflectors are applied in the 1D SAIR to compress the antenna beam for achieving the high-resolution on the Y_r axis [16]. However, the SAIRs with the large reflector usually have a larger volume and are not suitable for many applications. The BP method uses the back projection method to perform the cumulative imaging with array rotating and can reconstruct the target image effectively. But for the near-field RS-SAIR with wider PSF and serious stacking interference between targets, the back projection method cannot deal with these problems effectively; its recovery precision is not good.

In this paper, we seek a better solution from another angle. For the given target S_i, when the array is rotating from 1 to 180° (rotating step is 1°), its projection coordinate x_{ri} can be expressed as

$$\begin{aligned} x_{ri}(\theta_a) &= R_i \cos(\theta_a + \theta_i) \\ R_i &= \sqrt{x_i^2 + y_i^2}, \quad \theta_i = \arctan\left(\frac{x_i}{y_i}\right) \end{aligned} \tag{10}$$

For the given target S_i, its R_i and θ_i are the constants, which depended on the target coordinates (x_i, y_i) only. Thus, the projection coordinate x_{ri} will change with the angle θ_a of antenna array, and its curve meets the cosine distribution. As Figure 3 shows, the images T^P are measured by RS-SAIR at a series of angle θ_a firstly (Figures 3(a) and 3(b)). Then, T^P are arranged to constitute the completed angle-orientation image (Figure 3(c)). Obviously, there are two cosine curves in the angle-orientation image.

Based on this fact, we can arrange the 1D projection images (with different θ_a) to constitute the angle-orientation image according the sequence of angle θ_a. Then the target will be extracted by the cosine matching method from angle-orientation image one by one. Due to the fact the weak targets are usually hidden in the projection of higher targets, the higher targets will be first s extracted partly for exposing the weak targets. Considering the interference noise between targets is higher for near-field RS-SAIR, the nearby targets of the higher target will be extracted at the same time. In addition, each target S_i will be extracted repeatedly in CMI method for maintaining the target continuity. Its detailed process can be summarized as follows:

(1) At the start of the CMI method, initialize the brightness temperature image $T_B = 0$ and draw the cosine

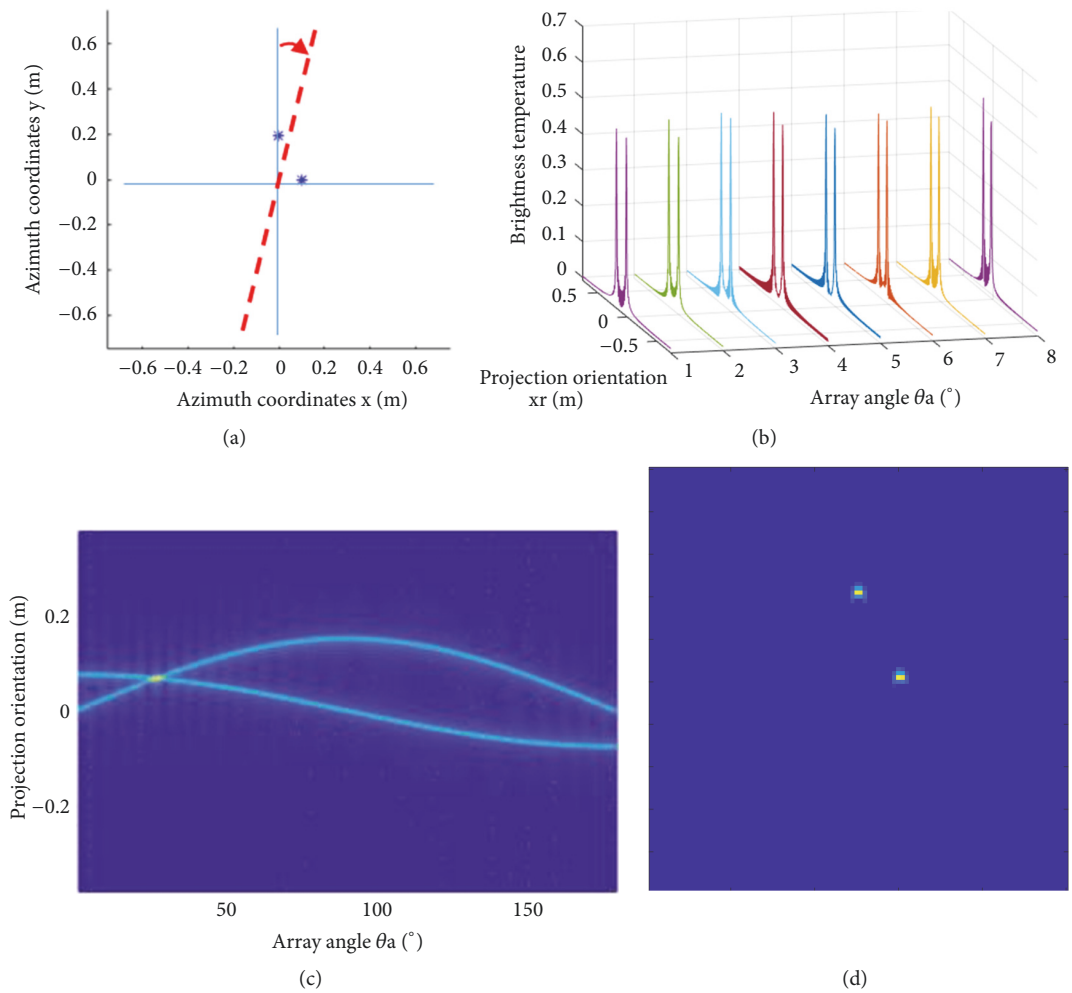

Figure 3: Demonstrative experiment of RS-SAIR. (a) Target scene. (b) The 1D projection images with θ_a=1~8°. (c) Completed angle-orientation image. (d) The reconstructed image.

images $T_{S\text{-}i}$ of each target S_i with same dimension (M, N) of angle-orientation image T_{ao}.

$$T_{S\text{-}i}(m,n) = \begin{cases} 1 & \text{when } m = R_i \cos(n+\theta_i) \\ 0 & \text{for other } (m,n) \end{cases} \tag{11}$$

where (R_i,θ_i) is the polar orientation of target S_i.

(2) At the kth step, calculate the correlation values $CV_{S\text{-}i}$ between image $T_{s\text{-}i}$ and remaining image $T_{ao\text{-}k}$ as $CV_{S\text{-}i}$ = sum[$T_{s\text{-}i}$. * $T_{ao\text{-}k}$]/N. Then find the highest target S_{k0} with max $CV_{S\text{-}k0}$ and its coordinate (x_{k0}, y_{k0}). Record the highest target S_{k0} as $T_B(x_{k0}, y_{k0})$= $T_B(x_{k0}, y_{k0})$+ $CV_{S\text{-}k0}$. Initial subtraction factor matrix SB=0.

(3) Subtract a fraction of target S_{k0} from image $T_{ao\text{-}k}$ in advance: $T_{ao\text{-}k}$ = $T_{ao\text{-}k}$ - $(\gamma^{\wedge 2} CV_{S\text{-}k0})T_{S\text{-}k0}$, where γ is the minus factor. Then update matrix SB as SB(x_{k0}, y_{k0})= $(1\text{-}\gamma)\gamma CV_{S\text{-}k0}$.

(4) Search the neighbourhood (contains N pixels) of the target $S_{k\,0}$. If the value $CV_{S\text{-}kn}$ of target S_{kn} is higher than the noise threshold V_{noise}, it will be considered as an effective target. Record its value $CV_{S\text{-}kn}$ and update $T_B(x_{kn}, y_{kn})$= $T_B(x_{kn}, y_{kn})$+ $CV_{S\text{-}kn}$. Then update SB (x_{kn}, y_{kn})=$\gamma CV_{S\text{-}kn}$.

(5) Perform the subtraction of all selected targets in the kth step to form the new remaining image $T_{ao\text{-}(k+1)}$

$$T_{ao\text{-}(k+1)} = T_{ao-k} - \sum_{j=k0}^{j=kn} \mathrm{SB}\left(x_j, y_j\right) T_{S\text{-}j} \tag{12}$$

(6) Repeat steps (2)-(5) until all the residual $CV_{S\text{-}i}$ are below the noise threshold V_{noise}. The final image T_B is the brightness temperature image.

The kth flowchart of CMI method is given in Figure 4. The core of this CMI method is the selection of γ, N, and V_{noise}. As a benefit from the parameter γ, target Si will be extracted repeatedly for reducing the aliasing impact between targets and maintaining the target continuity. We know that a higher value of γ can be further reduced the complexity with fewer steps to reach the noise floor. However, the higher

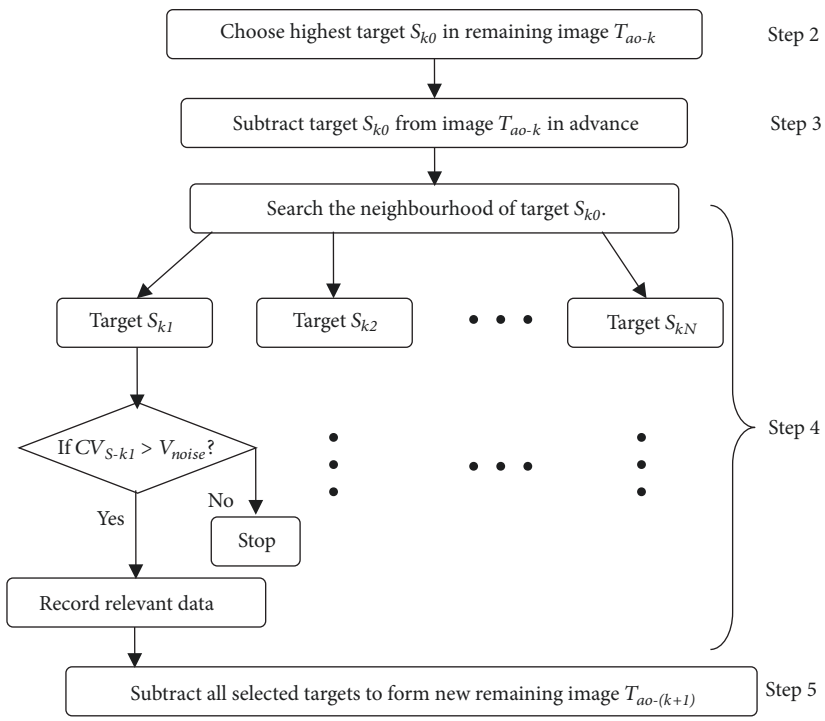

Figure 4: The kth flowchart of CMI method.

γ is only suitable for simple point targets. For the real-life extended target, the higher γ will lead to the result that some smaller targets will be canceled before be extracted. For our simulations, γ is selected by the following formula adaptively:

$$\gamma = 1 - \sqrt{mean\left(T_{ao}\right)} \tag{13}$$

where $mean(\bullet)$ represents to calculate the mean of normalized image T_{ao}. Clearly, the value of γ is smaller for real-life target with continuous distribution, and is larger for discrete isolated target. The parameters N and V_{noise} are the important factor for the search step (4). The larger N and smaller V_{noise} can reduce the time and complexity of CMI method, but the accuracy will be reduced too. Based on a large number of simulation experiments, we have come to the conclusion that N is usually selected as 2 times of the PSF's main-lobe width ($N = 10$ in this paper). And the noise threshold V_{noise} is usually set from 0.1 to 0.2. Figure 3(d) gives the images reconstructed by CMI method for the above two-point scene. It can be seen that two-point targets are reconstructed clearly by CMI method.

4. Simulation Experiments and Results

To verify the validity of the proposed CMI method, many numerical simulation experiments with various scenes have been conducted, and only a few representative ones are demonstrated in this section. The main simulation parameters are listed in Table 1. As Table 1 show, the RS-SAIR only needs 16 antennas to constitute the sparse linear array with the larger synthesis aperture. The antennas locations are set based on [29]; its arrangement is shown in Figure 5. The minimum baseline spacing is about 1.1cm, and the synthesis aperture D_{SA} is about 1 m. Then the array rotated around the center to achieve two-dimensional scene detection. That is to say RS-SAIR can achieve the equivalent imaging performance with fewer antennas (about 15% of the "T" array) in theory, and the ratio will be lower for the larger synthesis aperture [29, 30]. In order to simulate RS-SAIR imaging process accurately, the received signals of antennas are obtained by integral operation of the radiation waves generated by all discrete sources, and the visibility samples are calculated by cross-correlated calculation between antennas. The spacing (ΔL) between sources is set to half of the spatial resolution.

Table 1: Simulation parameters of RS-SAIR with a sparse array.

Parameters	Value	Parameters	Value
Antenna number	16	Rotation angle (θa)	1-180°
Wavelength (λ)	3mm	Rotating step ($\Delta\theta$)	2°
Synthesis aperture (D_{SA})	1m	Target spacing (ΔL)	4.5mm
Baseline spacing (Δu)	1.1cm	Imaging distance (R)	3m

In the reconstruction process, the 1D projection images are recovered by the MFFT method firstly. Then the proposed CMI method and BP method are applied to reconstruct the scene images from the 1D projection images. In addition, the NUFFT method [19] is also be applied to reconstruct the images from the irregular visibility function for comparison. All the experiments are performed in MATLAB software. The packaged presentation files used to support the findings of this paper are available from the corresponding author upon request.

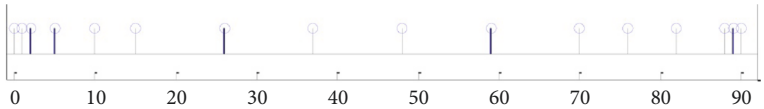

Figure 5: The arrangement of linear sparse array with 16 antennas (abscissa unit is Δu).

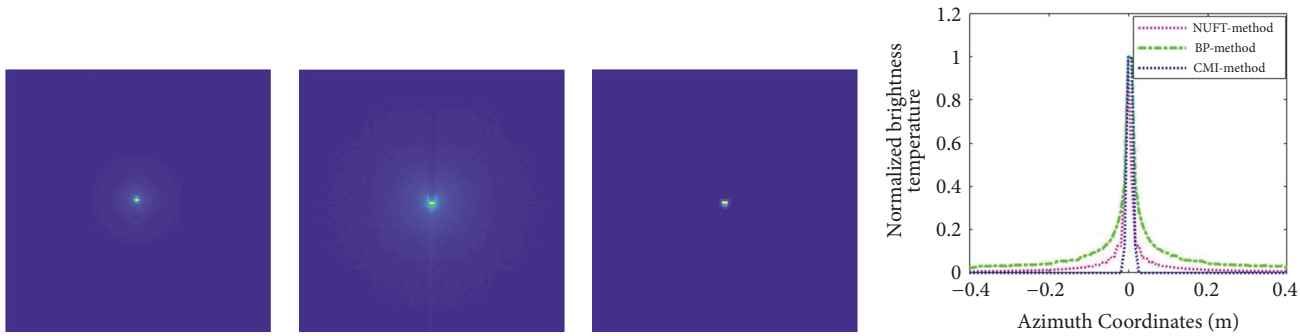

(a) (b) (c) (d)

Figure 6: Simulation results of PSF. (a) NUFFT's PSF. (b) BP's PSF. (c) CMI's PSF. (d) Sectional view of three PSFs.

4.1. Simulation Experiments of the Point Targets. Here, a series of simulation experiments with point targets are carried out to validate the imaging performance of the proposed CMI method for RS-SAIR. It is well known that the point spread function (PSF) is an important parameter for evaluating the resolution of imaging systems. We first make a simulation experiment with a point target. The corresponding results are demonstrated in Figure 6.

It can be seen from the PSF images that the shape of three PSFs is different. The NUFFT's PSF is a circular distribution (Figure 6(a)) with a fewer noise near the point. The BP's PSF is similar to the NUFFT's PSF distribution, but the noise near the point is higher. This is because that the 1D projection images reconstructed by the FFT method usually have higher side-lobe near the targets, then the 1D images are directly used to generate the final image in the BP method by the back projection method. This makes the side-lobe will also focus on the point target just as shown in Figure 6(b). In the proposed CMI method, these side-lobes will be eliminated when the higher target's cosine images $T_{s\text{-}i}$ are subtracted from image T_{ao} with its nearby targets. As shown in Figure 6(c), the CMI's PSF is similar to a point distribution compared with the ones of NUFFT and BP, and the noise is eliminated well. For comparing specifically, the 1D sectional view of three PSF images is demonstrated in Figure 6(d). Obviously, CMI's PSF is closer to a point target. Since the interpolation operation when resampling the visibility function, there is a fewer Gaussian noise near the point target in NUFFT's PSF. The BP's PSF is the worst one with the higher cumulative side-lobe noise.

For further testing the resolution of the proposed CMI method, a simulation experiment with two-point targets is performed as follows. The space of two-point targets is just the system resolution (i.e., 2ΔL), and the simulation results are shown in Figure 7.

As Figure 7 shows, the two-point targets have two cosine curves in the angle-orientation image clearly (Figure 7(a)). However, the images reconstructed by NUFFT and BP method are not very clear; there is a bigger side-lobe noise between two-point targets. It is difficult to distinguish the two points from the Figures 7(b) and 7(c). Actually, as the number of targets increases, this side-lobe noise will increase further. Through the multiple subtraction of higher targets, this side-lobe noise can be eliminated well by the CMI method, the two-point targets can be distinguished from the CMI reconstructed image (Figure 7(d)). This does mean that the imaging accuracy of RS-SAIR can be enhanced by the proposed CMI method effectively.

4.2. Simulation Experiments of the Extended Targets. For further demonstrating the imaging performance of the proposed CMI method, the 2D simulation experiments with extended targets are performed here. The target scene radiation intensity (brightness temperature) images are shown in Figures 8(a) and 9(a), with their gray value as the amplitude of the discrete point targets, and the distance between point targets is set as ΔL. The corresponding reconstructed images are shown in Figures 8(b)–8(d) and 9(b)–9(d).

It can be seen from the simulation results that the images reconstructed by the NUFFT and BP methods have serious noise pollution near the target caused by the serious side-lobe and interference between targets (Figures 8(b), 8(c), 9(b), and 9(c)). Since the BP method reconstructs the images from 1D projection images with higher noise directly, its reconstructed images are fuzzy. Some weaker targets are even covered by higher noises. Compared to BP's images, more target information are reconstructed from the resampling visibility function as shown in Figures 8(b) and 9(b). However, due to the influence of resampling error and lack of corresponding noise filtering means, the serious noise pollution still exists in the NUFFT's images. As a benefit from the multiple extraction operations of block target, these interference noises can be eliminated by the proposed CMI method effectively. As

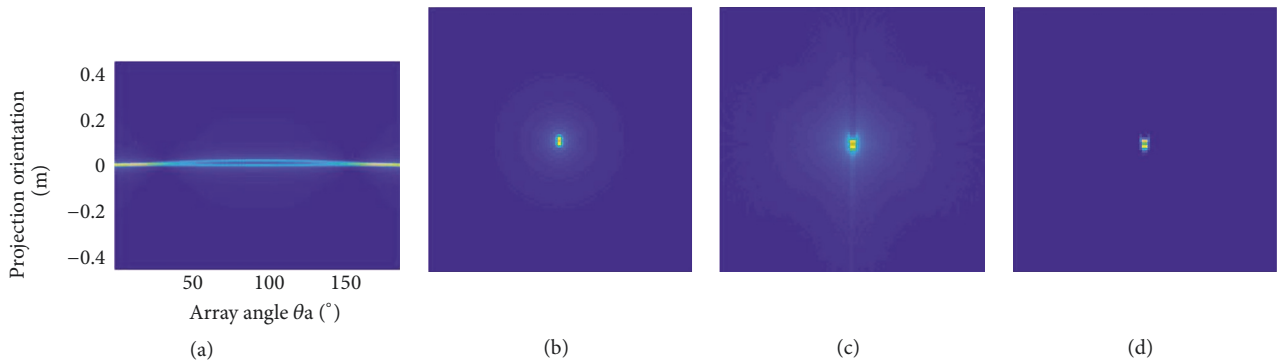

Figure 7: Simulation results of two-point targets. (a) The angle-orientation image. (b) The result of NUFFT method. (c) The result of BP method. (d) The result of CMI method.

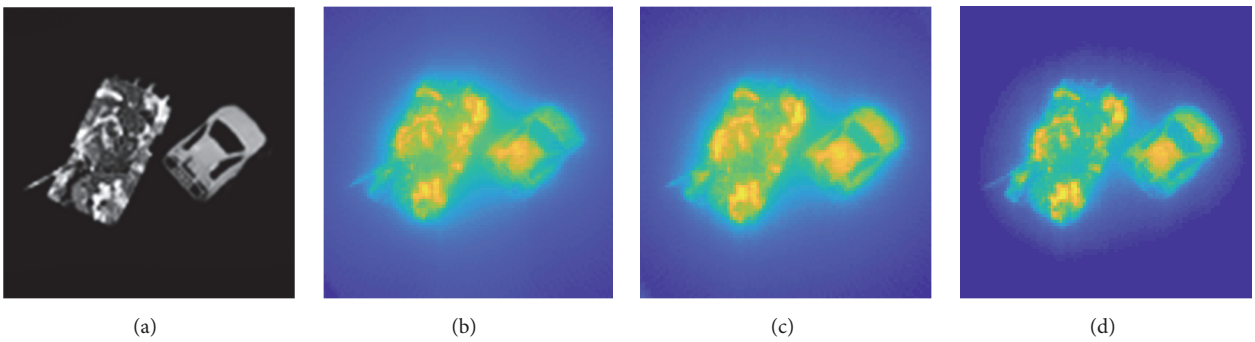

Figure 8: Simulation results of Tank&Car. (a) Original image. (b) The NUFFT's reconstructed image. (c) The BP's reconstructed image. (d) The CMI's reconstructed image.

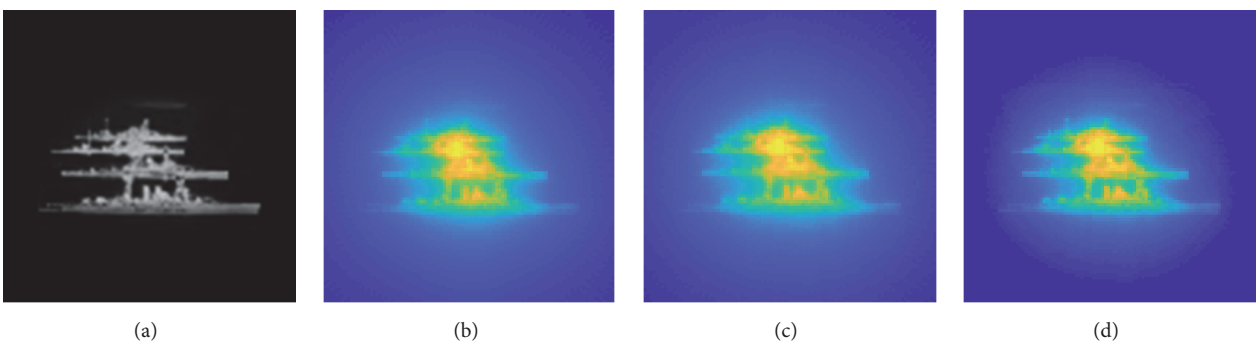

Figure 9: Simulation results of Boats. (a) Original image. (b) The NUFFT's reconstructed image. (c) The BP's reconstructed image. (d) The CMI's reconstructed image.

shown in Figures 8(d) and 9(d), the images reconstructed by CMI method are more clearer; the noise is well eliminated while the target information is well preserved. For comparing specifically, the sectional drawing (the middle row) of the reconstructed images (Figures 8(b)–8(d) and 9(b)–9(d)) is demonstrated in Figure 10. Obviously, the noise pollution around target of CMI method is lower than the NUFFT and BP method, and its target information is closer to the real target.

In order to compare the simulation results objectively, the structural similarity (SSIM), peak signal-to-noise ratio (PSNR) of images (Figures 8 and 9) and the root-mean square errors (RMSE) of the sectional drawing (Figure 10) are calculated by the following formula:

$$RMSE\left(T', T\right) = \frac{\sqrt{\sum_{i,j}\left[T'\left(i,j\right) - T\left(i,j\right)\right]^2}}{\sqrt{\sum_{i,j} T\left(i,j\right)^2}} \tag{14}$$

$$SSIM\left(T', T\right) = \frac{\left(2\mu_{T'}\mu_T + C_1\right)\left(\sigma_{T'T} + C_2\right)}{\left(\mu_{T'}^2 + \mu_T^2 + C_1\right)\left(\sigma_{T'}^2 + \sigma_T^2 + C_2\right)} \tag{15}$$

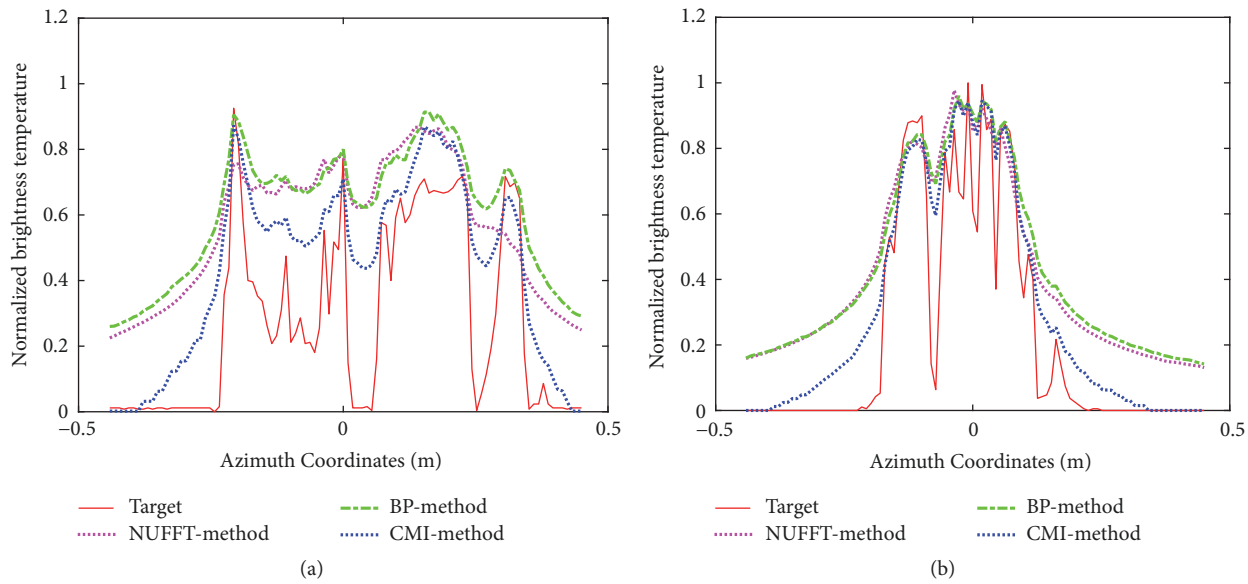

Figure 10: 1D sectional drawing of two-target scene. (a) Sectional drawing of Tank&Car. (b) Sectional drawing of Boats.

$$PSNR\left(T', T\right) = 10 \cdot \log_{10} \frac{\max\left(T\right)^2}{\sum_{i=1,j=1}^{i=M,j=N} \left(\left[T'\left(i,j\right) - T\left(i,j\right)\right]^2 / \left(M \times N\right)\right)} \quad (16)$$

where T' is the reconstructed image and T is the original one. $\mu_{T'}$ and μ_T are the mean of image T' and T separately. $\sigma_{T'}$ and σ_T are the standard deviation of image T' and T, respectively. $\sigma_{T'T}$ is the covariance of image T' and T. C_1 and C_2 are the smallest positive constants. $\max(T)$ denotes to find the max value of the original image T.

The corresponding calculation results are presented in Table 2. Clearly, the images of CMI have the highest SSIM and PSNR, and the RMSE of CMI method is also the lowest one. This indicates that the proposed CMI method can realize a higher imaging accuracy for RS-SAIR and reconstruct the target information accurately while reducing the noise.

Table 2: Comparison of objective data between NUFFT, BP, and CMI methods.

Target scene	Tank&car			Boats		
	RMSE	SSIM	PSNR	RMSE	SSIM	PSNR
NUFFT	0.1683	0.2733	10.6947	0.1288	0.2205	13.7518
BP	0.1730	0.2568	9.7559	0.1345	0.2102	13.0721
CMI	0.1449	0.7256	16.9164	0.1162	0.6893	18.9312

5. Conclusion

RS-SAIR with linear sparse array can utilize some small aperture antennas to realize high-resolution 2D imaging observation. However, due to lack of matched imaging method, its imaging precision is usually low. For improving the imaging accuracy of RS-SAIR further, a novel imaging method (named Cosine Matching Imaging (CMI)) is proposed in this paper. In CMI method, the 1D projection images are reconstructed by the MFFT method at every angle firstly. Then, the 1D projection images are arranged to constitute an angle-orientation image according the measured angle. The brightness temperature image will be extracted by the CMI method from the angle-orientation image in the end. For reducing interference noise of RS-SAIR and maintaining the target continuity, each target is extracted with its nearby targets repeatedly in CMI method. The effectiveness of the proposed CMI is validated by the simulation experiments. The simulation results demonstrate that the CMI method can realize a higher imaging accuracy for RS-SAIR; the images reconstructed by CMI method are clearer than that by NUFFT and BP methods. The imaging error caused by the interference between targets is eliminated well by the proposed CMI method. In addition, although the proposed CMI method is analyzed and verified in near-field condition in this paper, it is also suitable for the far-field RS-SAIR.

Data Availability

All our experiments are performed in MATLAB software. The packaged presentation files used to support the findings of this paper are available from the corresponding author upon request.

Conflicts of Interest

The authors declare that there are no conflicts of interest regarding the publication of this article.

Acknowledgments

This work is supported by National Natural Science Foundation of China (61601237 and 61671149), Jiangsu Provincial

Natural Science Foundation of China (BK20160901), Natural Science Foundation of Jiangsu Higher Education Institutions of China (16KJB420001), and NUPTSF (NY215042).

References

[1] S. Demirci, H. Cetinkaya, E. Yigit, C. Ozdemir, and A. A. Vertiy, "A study on millimeter-wave imaging of concealed objects: application using backprojection algorithm," *Progress in Electromagnetics Research*, vol. 128, no. 1, pp. 457–477, 2012.

[2] R. Appleby and R. N. Anderton, "Millimeter-wave and submillimeter-wave imaging for security and surveillance," *Proceedings of the IEEE*, vol. 95, no. 8, pp. 1683–1690, 2007.

[3] H.-M. Chen, S. Lee, R. M. Rao, M.-A. Slamani, and P. K. Varshney, "Imaging for concealed weapon detection," *IEEE Signal Processing Magazine*, vol. 22, no. 2, pp. 52–61, 2005.

[4] D. M. Le Vine, M. Kao, A. B. Tanner, C. T. Swift, and A. Griffis, "Initial Results in the Development of a Synthetic Aperture Microwave Radiometer," *IEEE Transactions on Geoscience and Remote Sensing*, vol. 28, no. 4, pp. 614–619, 1990.

[5] C. S. Ruf, C. T. Swift, A. B. Tanner, and D. M. Le Vine, "Interferometric synthetic aperture microwave radiometry for the remote sensing of the earth," *IEEE Transactions on Geoscience and Remote Sensing*, vol. 26, no. 5, pp. 597–611, 1988.

[6] B. Lambrigtsen, W. Wilson, A. Tanner, T. Gaier, C. Ruf, and J. Piepmeier, "GeoSTAR - A microwave sounder for geostationary satellites," in *Proceedings of the 2004 IEEE International Geoscience and Remote Sensing Symposium Proceedings: Science for Society: Exploring and Managing a Changing Planet. IGARSS 2004*, pp. 777–780, September 2004.

[7] F. Torres, A. B. Tanner, S. T. Brown, and B. H. Lambrigsten, "Robust array configuration for a microwave interferometric radiometer: Application to the GeoSTAR project," *IEEE Geoscience and Remote Sensing Letters*, vol. 4, no. 1, pp. 97–101, 2007.

[8] K. Rautiainen, J. Kainulainen, T. Auer, J. Pihlflyckt, J. Kettunen, and M. T. Hallikainen, "Helsinki university of technology L-B and airborne synthetic aperture radiometer," *IEEE Transactions on Geoscience and Remote Sensing*, vol. 46, no. 3, pp. 717–726, 2008.

[9] J. Wu, C. Zhang, H. Liu, and W. Sun, "Asynchronous rotation scan for synthetic aperture interferometric radiometer," *Science China Technological Sciences*, vol. 52, no. 6, pp. 1735–1743, 2009.

[10] A. Hu and J. Miao, "A method to enlarge the FOV for 8 mm band synthetic aperture radiometer," *Journal of Infrared, Millimeter and Terahertz Waves*, vol. 32, no. 1, p. 50, 2013.

[11] A. Tanner, T. Gaier, W. Imbriale, P. Kangaslahti, B. Lambrigtsen, and B. Lim, "A dual-gain design for the geostationary synthetic thinned array radiometer," *IEEE Geoscience and Remote Sensing Letters*, vol. 11, no. 8, pp. 1340–1344, 2014.

[12] C. Zhang, H. Liu, J. Wu et al., "Imaging analysis and first results of the geostationary interferometric microwave sounder demonstrator," *IEEE Transactions on Geoscience and Remote Sensing*, vol. 53, no. 1, pp. 207–218, 2015.

[13] M. Martín-Neira, D. M. Levine, Y. Kerr et al., "Microwave interferometric radiometry in remote sensing: An invited historical review," *Radio Science*, vol. 49, no. 6, pp. 415–449, 2014.

[14] C. Zhang, J. Wu, and H. Liu, "Clock Scanning Microwave Interferometric Radiometer and Potential Application Analysis," *IEEE Journal of Selected Topics in Applied Earth Observations and Remote Sensing*, vol. 8, no. 9, pp. 4262–4272, 2015.

[15] J. Wu, C. Zhang, H. Liu, and J. Yan, "Performance Analysis of Circular Antenna Array for Microwave Interferometric Radiometers," *IEEE Transactions on Geoscience and Remote Sensing*, vol. 55, no. 6, pp. 3261–3271, 2017.

[16] K. Chen, Y. Zhu, X. Guo et al., "Design of 8mm-band aperture synthetic radiometer and imaging experiment," *Journal of Infrared, Millimeter, and Terahertz Waves*, vol. 31, no. 6, pp. 724–734, 2010.

[17] L. Niu, H. Liu, L. Wu, and J. Wu, "Experimental study of an L-band synthetic aperture radiometer for ocean salinity measurement," in *Proceedings of the 36th IEEE International Geoscience and Remote Sensing Symposium, IGARSS 2016*, pp. 418–421, China, July 2016.

[18] X. Zhou, H. Sun, J. He, and X. Lu, "NUFFT-Based iterative reconstruction algorithm for synthetic aperture imaging radiometers," *IEEE Geoscience and Remote Sensing Letters*, vol. 6, no. 2, pp. 273–276, 2009.

[19] J. A. Fessler and B. P. Sutton, "Nonuniform fast Fourier transforms using min-max interpolation," *IEEE Transactions on Signal Processing*, vol. 51, no. 2, pp. 560–574, 2003.

[20] L. Feng, Q. Li, K. Chen et al., "The gridding method for image reconstruction of nonuniform aperture synthesis radiometers," *IEEE Geoscience and Remote Sensing Letters*, vol. 12, no. 2, pp. 274–278, 2015.

[21] A. Camps, M. Vall-llossera, I. Corbella, F. Torres, and N. Duffo, "Angular and Radiometric Resolution of Y-Shaped Nonuniform Synthetic Aperture Radiometers for Earth Observation," *IEEE Geoscience and Remote Sensing Letters*, vol. 5, no. 4, pp. 793–795, 2008.

[22] Y. F. Shao, R. Wang, Y. K. Deng et al., "Fast backprojection algorithm for bistatic SAR imaging," *IEEE Geoscience and Remote Sensing Letters*, vol. 10, no. 5, pp. 1080–1084, 2013.

[23] S. Ha and K. Mueller, "A Look-Up Table-Based Ray Integration Framework for 2-D/3-D Forward and Back Projection in X-Ray CT," *IEEE Transactions on Medical Imaging*, vol. 37, no. 2, pp. 361–371, 2018.

[24] F.-L. Sun, S.-W. Zhang, H. Liu, and C. Zhang, "Resolution and radiometric sensitivity analysis of the rotating synthetic aperture radiometer based on filtered back projection algorithm," *Dianzi Yu Xinxi Xuebao/Journal of Electronics and Information Technology*, vol. 36, no. 6, pp. 1413–1418, 2014.

[25] J. Chen, Y. Li, J. Wang, Y. Li, and Y. Zhang, "Adaptive CLEAN algorithm for millimetre wave synthetic aperture imaging radiometer in near field," *IET Image Processing*, vol. 9, no. 3, pp. 218–225, 2015.

[26] A. Tanner, B. Lambrigsten, T. Gaier, and F. Torres, "Near Field Characterization of the GeoSTAR Demonstrator," in *Proceedings of the 2006 IEEE International Symposium on Geoscience and Remote Sensing*, pp. 2529–2532, Denver, CO, USA, July 2006.

[27] J. Chen, Y. Li, J. Wang, Y. Li, and Y. Zhang, "An accurate imaging algorithm for millimeter wave synthetic aperture imaging radiometer in near-field," *Progress in Electromagnetics Research*, vol. 141, pp. 517–535, 2013.

[28] R. Butora, M. Martín-Neira, and A.-L. Rivada-Antich, "Fringe-washing function calibration in aperture synthesis microwave radiometry," *Radio Science*, vol. 38, no. 2, pp. 15/1–15/15, 2003.

[29] A. Camps, A. Cardama, and D. Infantes, "Synthesis of large low-redundancy linear arrays," *IEEE Transactions on Antennas and Propagation*, vol. 49, no. 12, pp. 1881–1883, 2001.

[30] J. Dong, Q. Li, R. Jin, Y. Zhu, Q. Huang, and L. Gui, "A method for seeking low-redundancy large linear arrays in aperture synthesis microwave radiometers," *IEEE Transactions on Antennas and Propagation*, vol. 58, no. 6, pp. 1913–1921, 2010.